

Hydrodynamics prediction of a ship in static and dynamic states

P. Du^{1a}, A. Ouahsine^{*1} and P. Sergent²

¹Laboratoire Roberval, UMR-CNRS 7337, Sorbonne Universités, Université de Technologie de Compiègne, Centre de recherches Royallieu, CS 60319, 60203 Compiègne cedex, France

²CEREMA-134, rue de Beauvais, CS 60039, 60200 Compiègne, France

(Received June 24, 2017, Revised July 10, 2017, Accepted July 12, 2017)

Abstract. The ship hydrodynamics in static and dynamic states were investigated using 3-dimensional numerical simulations. The static case simulated a fixed ship, while the dynamic case considered a ship with free sinkage and trim using the mesh morphing technique. High speed was found to increase the wave elevation around the ship. Compared with the static case, the dynamic case seemed to generate higher waves near the bow and after the stern. The frictional resistance was found to be more dominant. However, the pressure resistance became gradually important with the increase of the ship speed. The trim and sinkage were also analyzed to characterize the ship hydrodynamics in the dynamic state.

Keywords: hydrodynamics; trim; sinkage; ship waves; advancing resistance

1. Introduction

Numerical methods, especially the Computational Fluid Dynamics (CFD) approach has become increasingly important and is now an indispensable part for ship dynamics research. The most attractive problems, including ship seakeeping, self-propulsion and maneuvering etc. have been realized by several works. Carrica *et al.* (2007) used an unsteady Reynolds-Averaged Navier-Stokes (RANS) solver to simulate the ship hydrodynamics. The free surface was captured with a single-phase level set method. Dynamic overset grid was used for the 6-DoF (degree of freedom) motions of the ship (Wilson *et al.* 2006). Shen *et al.* (2015) implemented the overset method into the open source CFD code OpenFOAM and simulated the turning circle and zig-zag maneuvers of a self-propelled ship. Recently, the Immersed Boundary Method (IBM) was also proposed to simulate the ship hydrodynamics (Huang *et al.* 2008). Although the accuracy needs to be improved, it is still promising to simulate moving boundary problems. Guo *et al.* (2012) predicted seakeeping of a KVLCC2 in head waves. RANS was proved to be more accurate than the strip theory in all wavelengths. The ship motions in restricted and shallow waters were also studied by several researchers (Tezdogan *et al.* 2016, Linde *et al.* 2016, Du *et al.* 2017, Toan *et al.* 2013).

*Corresponding author, Professor, E-mail: ouahsine@utc.fr

^aPh.D. Student, E-mail: pp1565156@126.com

According to these works, CFD method is proven to be extremely suitable for ship dynamics problems. RANS (Reynolds-Averaged Navier-Stokes) seems a good choice regarding both the computational capability and precision. The free surface can be captured either using the level set or the Volume of Fluid (VOF) approach. With respect to the moving ship problems, mesh morphing techniques, remeshing method, overset method or IBM are all possible, depending on the large or small deformations.

In this study, the effect of the dynamic draft on ship hydrodynamics is investigated by coupling an Unsteady Reynolds-Averaged Navier-Stokes (URANS) based CFD solver with a 2DOF-rigid body model. The effects of free heave and pitch are considered using the mesh morphing. Two conditions of the ship with and without the free sinkage and trim are simulated. The wave elevations, ship resistance, trim and sinkage are analyzed, and the results are validated using the experimental benchmarks.

2. Numerical methods

2.1 Hydrodynamic equations

To simulate the flow around the ship, the URANS equations with VOF (Volume of Fluid) method are solved by using the OpenFOAM open source code. The governing equations read (Du *et al.* 2017)

$$\nabla \cdot \mathbf{U} = 0 \quad (1)$$

$$\frac{\partial \rho \mathbf{U}}{\partial t} + \nabla \cdot [\rho(\mathbf{U} - \mathbf{U}_g)\mathbf{U}] = -\nabla p_{\text{rgh}} - \mathbf{g} \cdot \mathbf{x} \nabla \rho + \nabla \cdot (\mu_{\text{eff}} \nabla \mathbf{U}) + (\nabla \mathbf{U}) \cdot \nabla \mu_{\text{eff}} + \mathbf{f}_\sigma \quad (2)$$

where \mathbf{U} is the fluid velocity, ρ is the fluid density. \mathbf{U}_g is the grid velocity taking into account the mesh motion. $p_{\text{rgh}} = p - \rho \mathbf{g} \cdot \mathbf{x}$ is a modified pressure, where \mathbf{x} is the position vector, g is the gravity acceleration. \mathbf{f}_σ is the surface tension term. $\mu_{\text{eff}} = \rho(\nu + \nu_t)$ denotes the effective dynamic viscosity, where ν and ν_t are the kinematic and eddy viscosities respectively. ν_t is obtained from a specific turbulence model. In this study, the SST (Shear Stress Transport) $k-\omega$ model (Menter 1993) is adopted. It is a two-equation eddy-viscosity model which combines the advantages of the $k-\varepsilon$ and $k-\omega$ models. The $k-\omega$ model is used in the boundary layer and the $k-\varepsilon$ model in the free stream flow. Thereby it is less sensitive to free stream conditions and has better performance predicting the flow separation and reattachment.

2.2 Multiphase model

The VOF approach is used for multiphase flow simulations, together with an artificial compression technique. The transport equation reads

$$\frac{\partial \alpha}{\partial t} + \nabla \cdot [\alpha(\mathbf{U} - \mathbf{U}_g)] + \nabla \cdot [\alpha(1 - \alpha)\mathbf{U}_r] = 0 \quad (3)$$

where α is the phase fraction, which takes values within the range $0 \leq \alpha \leq 1$. $\alpha = 0$ and $\alpha = 1$

correspond with gas and liquid respectively. It can be seen that the compression term (the last term on the left-hand side) only takes effect within the interface. This term is able to compress the free surface towards a sharper one. $\mathbf{U} = \alpha\mathbf{U}_w + (1-\alpha)\mathbf{U}_a$ is the effective velocity, and $\mathbf{U}_r = \mathbf{U}_w - \mathbf{U}_a$ is the relative velocity between the two phases, where the subscripts ‘w’ and ‘a’ denote water and air respectively. The density and dynamic viscosity are calculated according to the following equations

$$\rho = \alpha\rho_w + (1-\alpha)\rho_a \quad (4)$$

$$\mu = \alpha\mu_w + (1-\alpha)\mu_a \quad (5)$$

The surface tension term f_σ is calculated as

$$\mathbf{f}_\sigma = \sigma\kappa\nabla\alpha \quad (6)$$

where σ is the surface tension coefficient (0.07 kg/s² in water). κ is the curvature of the free surface interface, determined from the volume of fraction by $\kappa = -\nabla \cdot (\nabla\alpha / |\nabla\alpha|)$.

2.3 Computational details

The solution procedure is presented in Fig. 1. The mesh information is updated at first. The 6-DoF rigid body motion solver is used to realize the mesh morphing, where the Newmark method is used for updating the mesh velocity and position. Following the dynamic mesh procedure, VOF and NS equations are solved continuously, where the pressure and velocity coupling is realized using the PIMPLE algorithm (Baniabedalruhman 2015). The turbulence is calculated at last to update the turbulent kinetic energy (k), specific dissipation (ω) and eddy viscosity (ν_t).

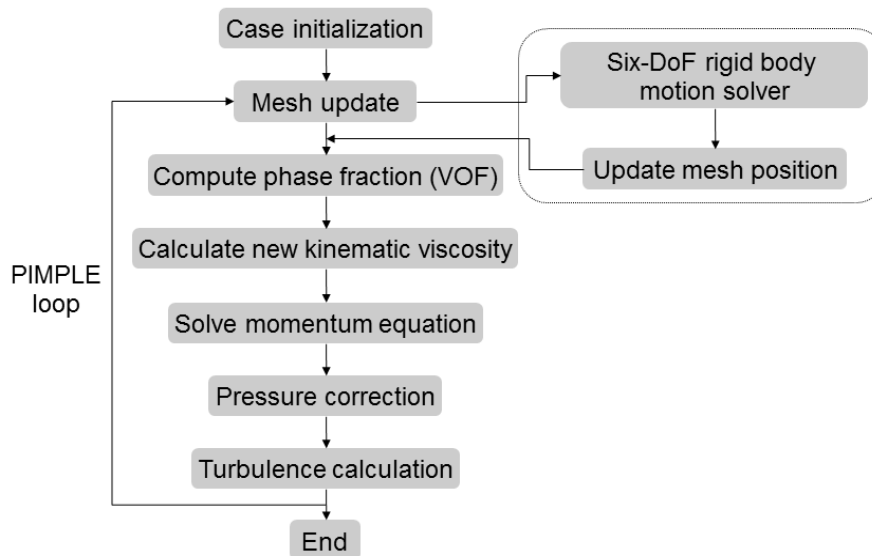


Fig. 1 Flowchart of the solution procedure

Normally a ship has 6-DOFs (Fig. 2), including three translational motions (surge, sway and heave) and three rotational motions (roll, pitch and yaw). Two cases are simulated and compared in this work, which are termed as the static and dynamic cases. The ship in the static case is fixed, where the grid velocity U_g is neglected in Eqs. (2)-(3). In the dynamic case, instead of 6-DOFs, only the heave and pitch motions are considered to limit the mesh deformation. The simulations are carried out on the Dell Precision Tower 7910 Workstation with 32 processors (Intel Xeon CPU E5-2640, 2.60 GHz).

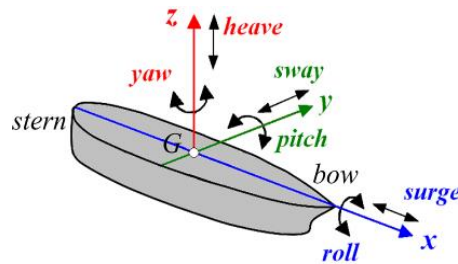


Fig. 2 6-DoF (degree of freedom) motions of the ship

Table 1 Geometrical parameters of the full-scale KRISO Container Ship (KCS) and model used in this study

Parameters	Symbols	Full scale	Model
Scale factor	γ		57.5
Length between perpendiculars	L_{PP} [m]	230	4
Beam	B [m]	32.2	0.5635
Draft	T [m]	10.8	0.1878
Displacement volume	∇ [m ³]	52,030	0.2737
Longitudinal center of buoyancy	L_{CB} (% L_{PP})	-1.48	-1.48
Wetted surface area without rudder	S_{W0} [m ²]	9424	2.8504
Moment of inertia	K_{xx}/B	0.4	0.4
	K_{yy}/B	0.25	0.25
	K_{zz}/B	0.25	0.25

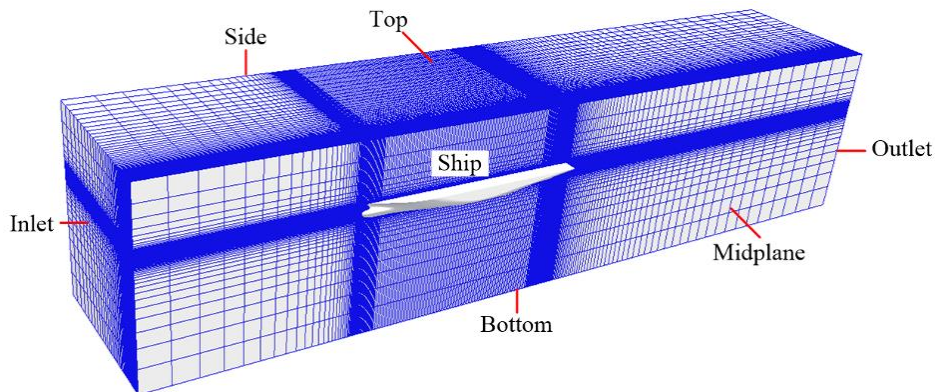


Fig. 3 Computational domain and boundary conditions

3. Computational domain and boundary conditions

The ship model used in this study is the KRISO Container Ship (KCS) developed by the Korea Research Institute for Ships and Ocean Engineering (KRISO). The geometrical parameters can be seen in Table 1. This is a well-tested ship model with many open experimental and numerical data. The computational domain is shown in Fig. 3, where the area containing the ship is refined to capture the flow field and the free surface. The bow and the stern are refined with a higher level since they have relatively more complex geometries. The detailed mesh generation procedure can be observed in Fig. 4. The background mesh is first generated. Then the meshes intersecting with the ship geometry will be split and snapped to the surface. Unused cells are removed during this process. Boundary layer meshes are added at last. Only a half domain in the y direction is simulated using the symmetry boundary condition to reduce the mesh number. Slip boundary conditions are used for the side, bottom and top of the domain.

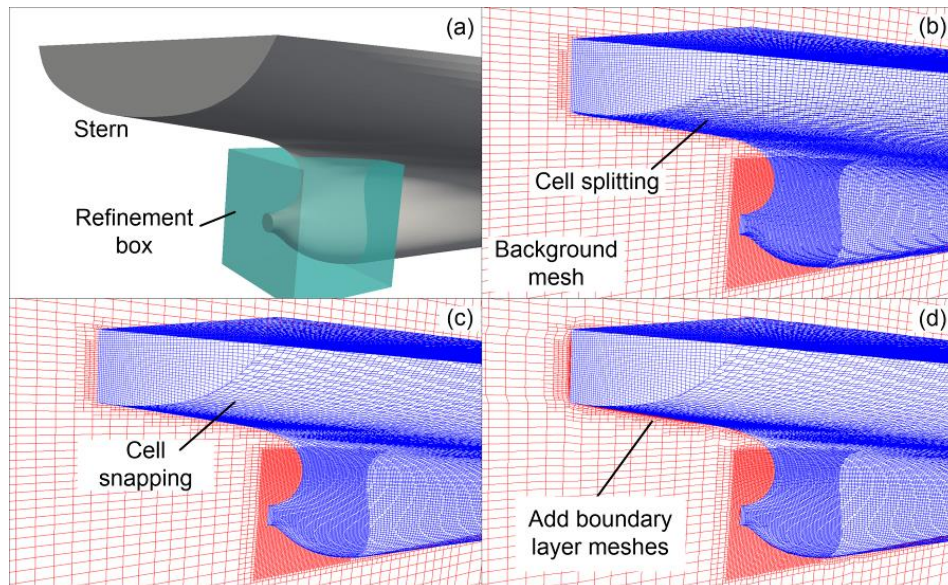


Fig. 4 Mesh generation procedures

4. Results and discussions

4.1 Grid sensitivity

Three different grids are used for the mesh sensitivity study with the mesh numbers 962,346, 1,485,916 and 1,717,375. They are denoted as grid 1, 2 and 3 respectively. The cases are carried out with the dynamic mesh. The mesh deformation can be clearly observed in Fig. 5. Only the meshes in the mesh morphing regions deforms during the simulation. The wave elevations at the lateral position $y/L_{pp}=0.0741$ are shown in Fig. 6. Only the wave profiles in the range of $0.3 < x/L_{pp} < 1.8$ are analyzed. The global convergence ratio R_m and the order of accuracy p_m are calculated according to the following equations (Ji *et al.* 2012, 2014)

$$R_m = \frac{\|\varepsilon_{32}\|_2}{\|\varepsilon_{21}\|_2} \quad p_m = \frac{\ln(\|\varepsilon_{32}\|_2 / \|\varepsilon_{21}\|_2)}{\ln(r)} \quad (7)$$

where r is the refinement ratio. $\|\varepsilon\|_2 = (\sum_{i=1}^N \varepsilon_i^2)^{1/2}$ denotes the L2 norm of the solution change over N points of the wave profile. The subscripts 1, 2 and 3 correspond to the three grid types. ε_{32} and ε_{21} represent the difference between a finer and a coarser grid. Two types of conditions can be analyzed using this method. When $R < 1$, the solution is convergent, and when $R > 1$, it is divergent. For our cases, R_m and p_m are 0.61 and 1.41 respectively, showing that our simulations are convergent.

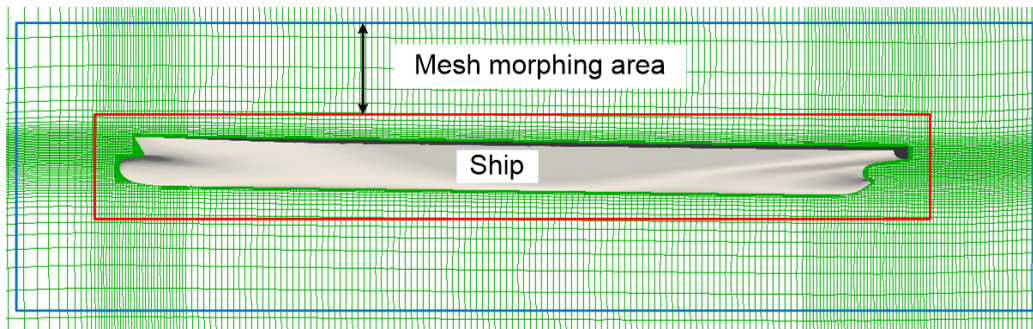


Fig. 5 Mesh morphing during the simulation

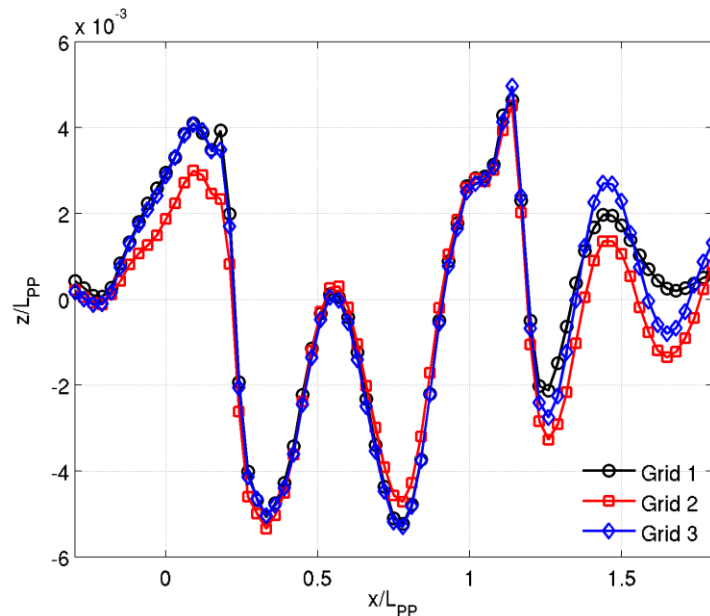


Fig. 6 Wave elevations at the lateral position $y/L_{PP}=0.0741$ for three different grids ($Fr=0.260$). The position values are normalized using the ship length (L_{PP})

The wave elevation contours with different mesh resolutions are shown in Fig. 7. It is obvious that the ship waves are simulated better with finer meshes. In Fig. 7(a), the waves near the bow and behind the ship are not resolved well, denoting the mesh is not fine enough. Comparatively, grid 2 and 3 can compute the waves and flow fields better, and grid 3 (Fig. 7(c)) is able to capture the waves far away from the ship. By balancing between the resolution of the physics and the computational time, grid 2 is selected throughout this study.

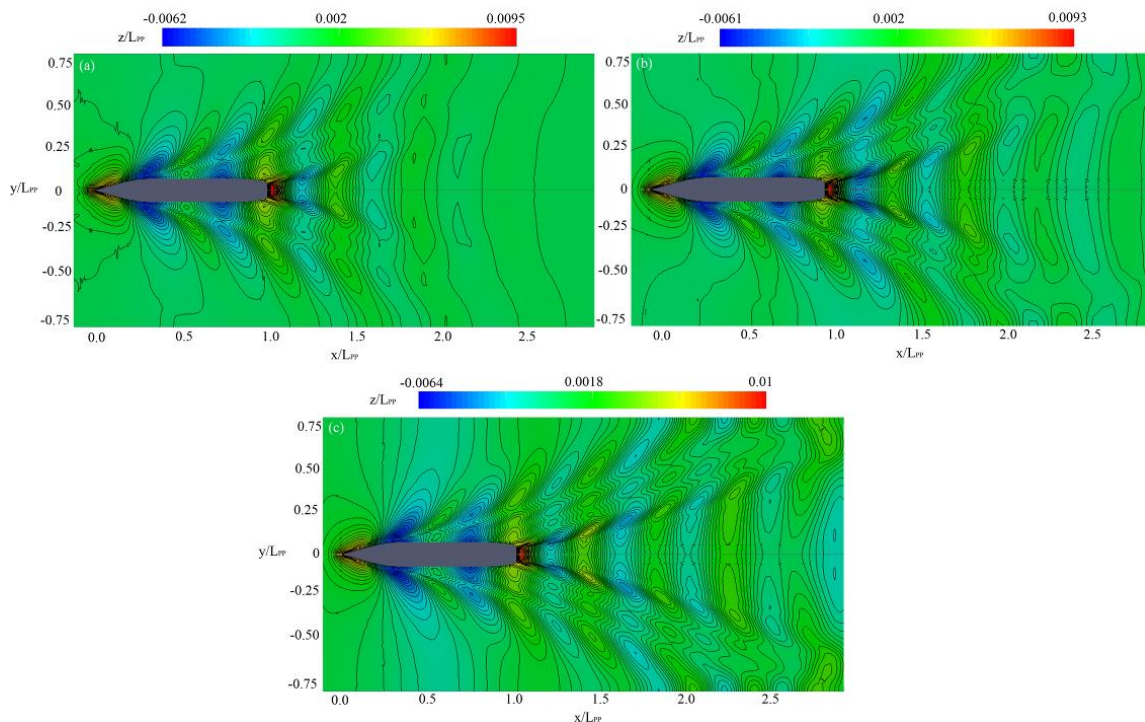


Fig. 7 Wave elevation contours with different mesh resolutions. (a) grid 1; (b) grid 2; (c) grid 3. The position values are normalized using the ship length (L_{PP})

4.2 Wave elevation analysis

The wave fields in the two cases are shown in Fig. 8, where classical Kelvin wave patterns are clearly observed. The wave contours in the static case (Fig. 8(b)) agree well with experiments (Hino 2005), proving that the mesh resolution is enough. The experiments were carried out for a towed ship similar to the setups in the static case. For the dynamic case (Fig. 8(c)), the wave field resembles that in the static case. However, the waves at the bow and near the stern are modified because of the sinkage and trim.

This modification is more obvious in the cross-section profiles at the lateral positions (y/L_{PP}) 0.0741, 0.1509 and 0.4224 in Fig. 9. It can be seen that the waves at the bow and behind the stern are elevated by the ship sinkage and trim. The difference in other positions is not obvious. And this difference diminishes gradually away from the ship.

The free surface on the hull is shown in Fig. 10. Because of the trim, the stern of the ship in the

dynamic case will be immersed more into the water, and the bow will be exposed more in the air. The wave elevations on the hull are extracted in Fig. 11. Similar with the results of Fig. 9, the differences between the two cases mainly lie at the bow and the stern. However, unlike the static case, the water level in the dynamic case will experience a fluctuation at the bow. It is clearer in Fig. 10 with the free surface. This is caused by the bulbous bow, which is able to manipulate the coming flow. Because of the trim, the stern is more submerged into water (Fig. 10). The wetted areas in the two cases are calculated in Fig. 12, where they are both larger than that in the initial state, showing that the moving ship will sink into the water. The dynamic case with free trim and sinkage corresponds with real situations. The wetted area in this case increases with a higher value than that in the static case. This is also the reason why it experiences higher resistance, which will be analyzed in the next section. In both cases, the area in water grows with the increase of the ship speed. Therefore, in reality, cautions should be taken when the ship is maneuvered with high speeds since the ship will continue sinking into the water.

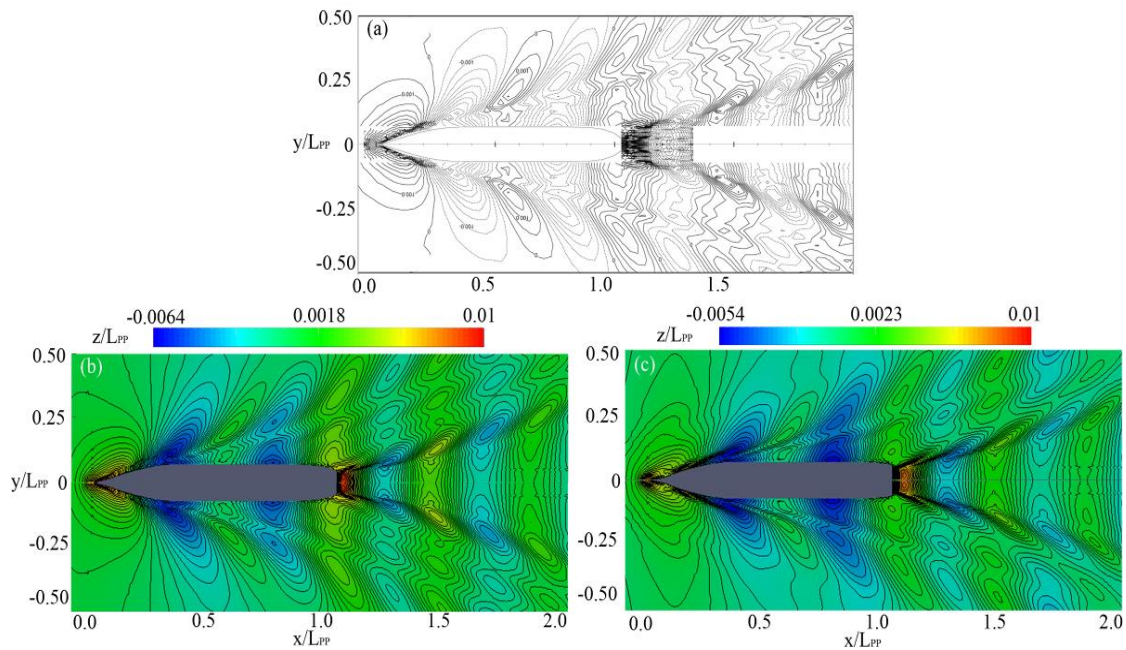


Fig. 8 Comparison of the wave elevation contours between the static and dynamic cases ($Fr=0.260$). (a) experiment (Hino 2005); (b) static case; (c) dynamic case. The position values are normalized using the ship length (L_{PP})

The wave elevations on the hull at three different speed ($Fr=0.227, 0.260, 0.282$) are shown in Fig. 11. It can be seen that the wave elevation grows with the increase of the ship speed. The largest wave elevations are near the bow and the stern. All the waves in the dynamic cases will have a fluctuation at the bow. However, the amplitude of this fluctuation reduces when the ship speed is increased. The extrema of the wave on the ship's side is pushed towards the stern by the accelerated flow. The ship-generated waves will also propagate further with a higher maneuvering speed.

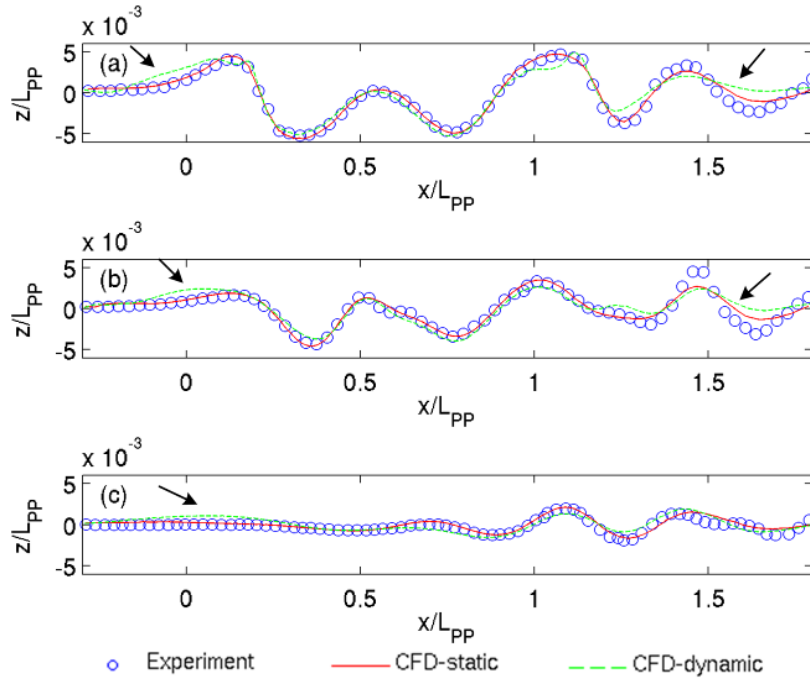


Fig. 9 Wave elevations at the lateral positions (a) $y/L_{PP}=0.0741$; (b) $y/L_{PP}=0.1509$; (c) $y/L_{PP}=0.4224$. The arrows point to the differences between the dynamic and static cases. The position values are normalized using the ship length (L_{PP}). Experimental data comes from Hino (2005)

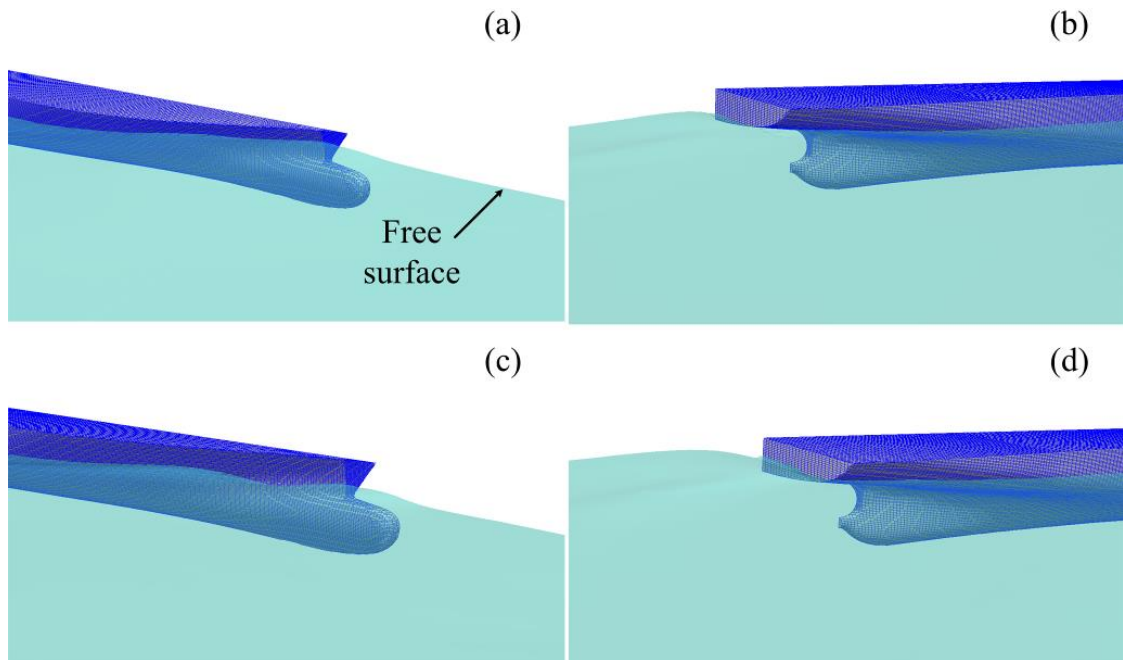


Fig. 10 Free surfaces at the bow and the stern. (a) and (b) concern the static case. (c) and (d) concern the dynamic case

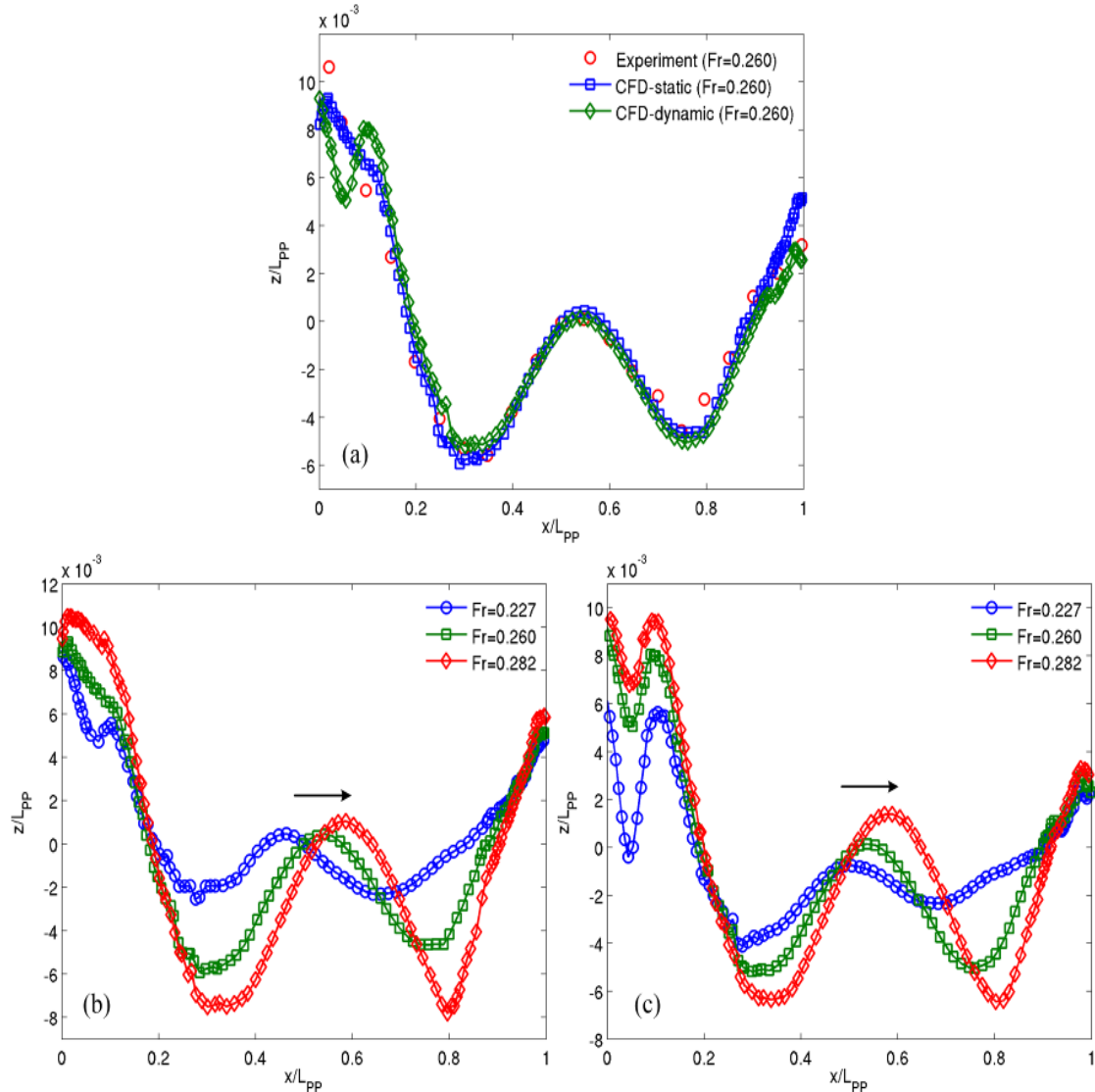


Fig. 11 Wave elevations on the hull surface. (a) Comparison between the static and dynamic cases ($Fr=0.260$); (b) wave elevations at three Froude numbers in the static case; (c) wave elevations at three Froude numbers in the dynamic case. The arrow points to the changing of the extrema of ship waves. Experimental data comes from Hino (2005). The position values are normalized using the ship length

Table 2 Ratios of the frictional (r_F) and pressure (r_P) resistances. $r_F = R_F/R_T$; $r_P = R_P/R_T$. R_T , R_F and R_P are the total, frictional and pressure resistances. Fr is the Froude number

Case	Resistance ratio [%]	$Fr=0.227$	$Fr=0.260$	$Fr=0.282$
Static	r_F	97.83	85.82	68.95
	r_P	2.17	14.18	31.05
Dynamic	r_F	96.82	85.66	68.04
	r_P	3.18	14.34	31.96

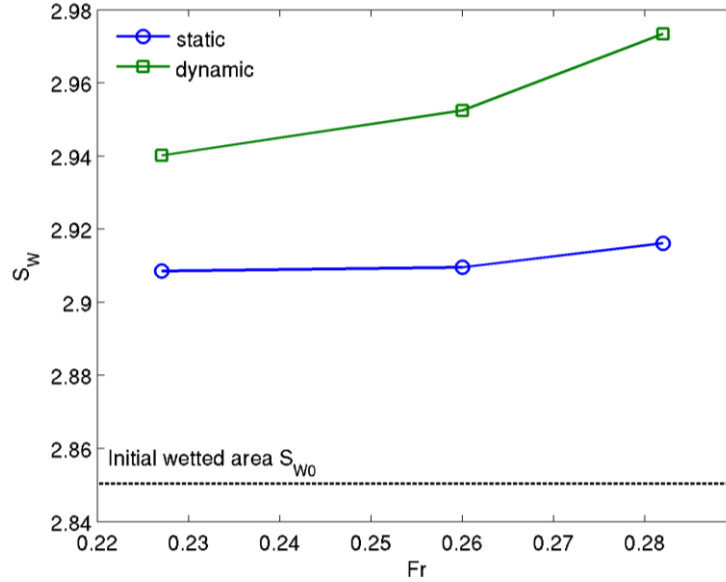


Fig. 12 Comparison of the wetted area (S_W) on the hull surface in the static and dynamic cases. Fr is the Froude number. S_{W0} is the initial wetted area

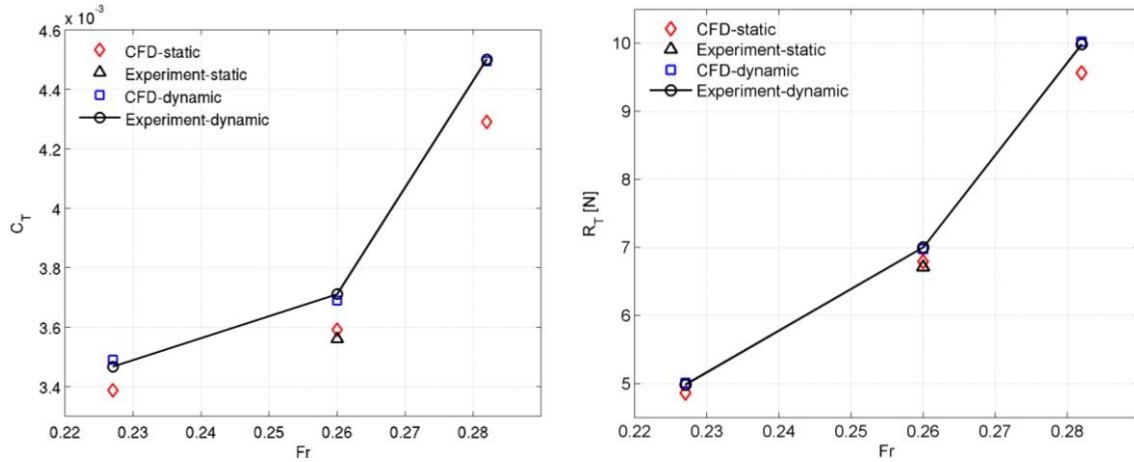


Fig. 13 Total resistance against the Froude number (Fr). C_T is the resistance coefficient. R_T is the total resistance. The experimental data comes from Hino (2005) and Kim *et al.* (2001)

4.3 Advancing resistance, sinkage and trim

In this study the resistance coefficients can be obtained using the following equations

$$C_T = \frac{R_T}{\frac{1}{2} \rho U^2 S_{W0}} \quad C_F = \frac{R_F}{\frac{1}{2} \rho U^2 S_{W0}} \quad C_P = \frac{R_P}{\frac{1}{2} \rho U^2 S_{W0}} \quad (8)$$

where C is the resistance coefficient. The subscripts 'T', 'F' and 'P' represent the total, frictional

and pressure resistances. S_{w0} is the wetted area of the ship at rest. It should be noted that for unsteady simulations, the forces on the ship are periodic even after convergence. The resistance should use the average value of at least one period. The final resistance coefficients are plotted in Fig. 13. The results agree well with experiments (Kim *et al.* 2001). For the dynamic case, the resistance is higher than that in the static case since it sinks more into the water. With the increase of the ship speed (Fr), the resistance increases. The ship resistance can be further divided into the frictional and pressure parts (Fig. 14). The frictional resistance is found to be more dominant than the pressure resistance in all cases. When the ship speed is increased, both will grow. Two factors will contribute to this phenomenon, the speed and the immersed area of the ship. The proportions of the two resistances are calculated to characterize their properties. In Table 2, the pressure resistance becomes increasingly important when the navigating speed of the ship increases, in both the dynamic and static cases.

As explained previously, compared with the static case, an important feature of the dynamic case is the allowance of the sinkage and trim. Their values are shown in Figs. 15-16, which are predicted close to experiments. The increase of the trim and sinkage are the reasons for the growing water levels and wetted areas on the ship hull. This will further influence the ship resistance.

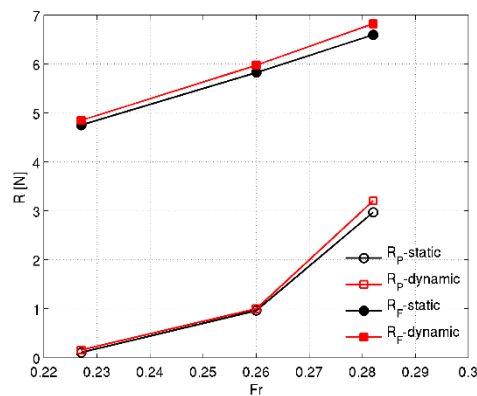


Fig. 14 Pressure (R_p) and frictional (R_f) resistances against the Froude number (Fr)

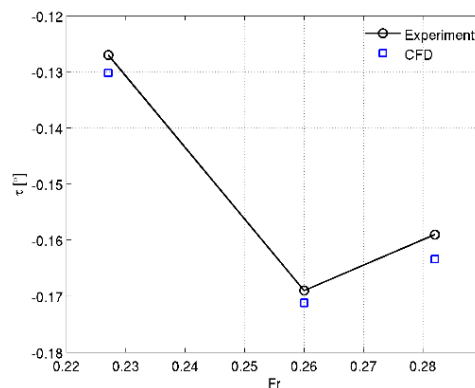


Fig. 15 Trim (τ) against the Froude number (Fr) in the dynamic case. Experimental data comes from Kim *et al.* (2001)

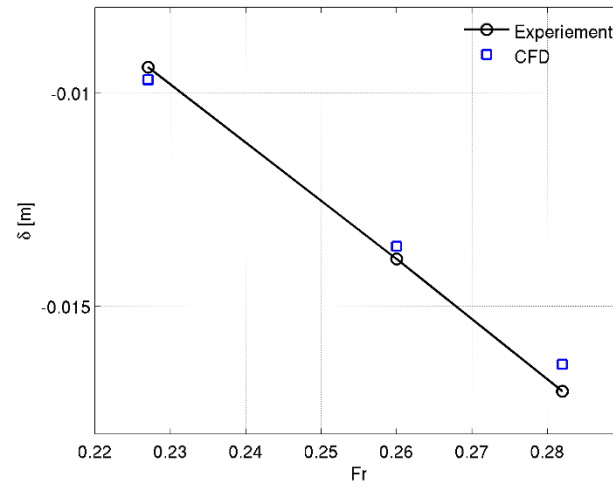


Fig. 16 Sinkage (δ) against Froude number (Fr) in the dynamic case. Experimental data comes from Kim *et al.* (2001)

5. Conclusions

The ship hydrodynamics with and without the trim and sinkage was simulated using 3-dimensional numerical simulations. The wave elevations and ship resistances were analyzed in depth to characterize the influence of the free trim and sinkage and the ship speed. When the ship speed was increased, the wave would grow and propagate further away from the ship. The waves at the bow and the stern were higher than that at other positions. Compared with the static case, the waves at the bow and after the stern in the dynamic case were observed to rise, while the wave change in other positions was not obvious. The waves at the bow in the dynamic case had a fluctuation, whose amplitude decreased with the increase of the ship speed.

The frictional and pressure resistances were extracted and analyzed separately. The frictional resistance was found to be dominant in all cases. However, the pressure resistance became progressively important with the growth of the ship speed. When the speed was higher, the ship sank more into the water with larger trim. Cautions should be taken when ships are practically maneuvered under this condition.

Acknowledgments

The research described in this paper was financially supported by the China Scholarship Council (CSC).

References

- Baniabedlruhman, A. (2015), "Dynamic meshing around fluid-fluid interfaces with applications to droplet tracking in contraction geometries", Ph.D. Dissertation, Michigan Technological University, U.S.A.
 Carrica, P.M., Wilson, R.V., Noack, R.W. and Stern, F. (2007), "Ship motions using single-phase level set

- with dynamic overset grids”, *Comput. Flu.*, **36**(9), 1415-1433.
- Du, P., Ouahsine, A. and Sergent, P. (2017), “Influence of the draft to ship dynamics in the virtual tank based on openfoam”, *Proceedings of the ECCOMAS Thematic Conference, VII International Conference on Computational Methods in Marine Engineering-Marine 2017*, Nantes, France, May.
- Du, P., Ouahsine, A., Toan, K.T. and Sergent, P. (2017), “Simulation of ship maneuvering in a confined waterway using a nonlinear model based on optimization techniques”, *Ocean Eng.*, **142**, 194-203.
- Guo, B., Steen, S. and Deng, G. (2012), “Seakeeping prediction of kvlcc2 in head waves with rans”, *Appl. Ocean Res.*, **35**, 56-67.
- Hino, T. (2005), *Proceedings of the cfd Workshop Tokyo 2005*, Tokyo, Japan.
- Huang, J., Carrica, P.M. and Stern, F. (2008), “Semi-coupled air/water immersed boundary approach for curvilinear dynamic overset grids with application to ship hydrodynamics”, *J. Numer. Meth. Flu.*, **58**(6), 591-624.
- Ji, S.C., Ouahsine, A., Smaoui, H. and Sergent, P. (2014), “3D numerical modeling of sediment resuspension induced by the compounding effects of ship-generated waves and the ship propeller”, *J. Eng. Mech.*, **140**(6), 04014034.
- Ji, S.C., Ouahsine, A., Smaoui, H. and Sergent, P. (2012), “3-d numerical simulation of convoy-generated waves in a restricted waterway”, *J. Hydrodyn. Ser. B*, **24**(3), 420-429.
- Kim, W., Van, S. and Kim, D. (2001), “Measurement of flows around modern commercial ship models”, *Exp. Flu.*, **31**(5), 567-578.
- Linde, F., Ouahsine, A., Huybrechts, N. and Sergent, P. (2016), “Three-dimensional numerical simulation of ship resistance in restricted waterways: Effect of ship sinkage and channel restriction”, *J. Waterw. Port C*, **143**(1), 06016003.
- Menter, F.R. (1993), *Zonal Two Equation k-Turbulence Models for Aerodynamic Flows*, AIAA paper 2906, 1993.
- Shen, Z., Wan, D. and Carrica, P.M. (2015), “Dynamic overset grids in openfoam with application to kcs self-propulsion and maneuvering”, *Ocean Eng.*, **108**, 287-306.
- Tezdogan, T., Incecik, A. and Turan, O. (2016), “Full-scale unsteady rans simulations of vertical ship motions in shallow water”, *Ocean Eng.*, **123**, 131-145.
- Toan, K.T., Ouahsine, A., Naceur, H. and Karima, W.E. (2013), “Assessment of ship manoeuvrability by using a coupling between a nonlinear transient manoeuvring model and mathematical programming techniques”, *J. Hydrodyn. Ser. B*, **25**(5), 788-804.
- Wilson, R.V., Carrica, P.M. and Stern, F. (2006), “Unsteady rans method for ship motions with application to roll for a surface combatant”, *Comput. Flu.*, **35**(5), 501-524.